

Image degradation due to different in-flight aero-optical environments

Matthew Kalensky[✉], Jonathan Wells, and Stanislav Gordeyev*

University of Notre Dame, Department of Aerospace and Mechanical Engineering,
Notre Dame, Indiana, United States

Abstract. High speed time-resolved wavefront and imaging measurements were taken synchronously in-flight through both boundary layer and shear layer environments around the Airborne Aero-Optical Laboratory for Beam Control. Instantaneous modulation transfer functions and point spread functions (PSFs), which characterize image degradation, were generated using wavefront data. Instantaneous power-in-bucket ratios were extracted from both the image data and computed from the wavefront data, and the ratios were found to correlate well with each other. The lower power-in-bucket values and related increased blurring that occurred predominantly in the streamwise direction were associated with large-scale, large-amplitude wavefront spatial variations due to large organized vortical structures present in the shear layer. The boundary layer did not create any significant image blurring due to the low level of aero-optical distortions. Finally, spatial autocorrelation functions were extracted from the wavefront data using the stitching method and were used to compute time-averaged PSFs for different aperture diameters. © 2020 Society of Photo-Optical Instrumentation Engineers (SPIE) [DOI: [10.1117/1.OE.59.10.104104](https://doi.org/10.1117/1.OE.59.10.104104)]

Keywords: imaging; wavefronts; aero-optics; point spread function; flight tests.

Paper 20200419 received Apr. 15, 2020; accepted for publication Oct. 1, 2020; published online Oct. 19, 2020.

1 Introduction

In many applications, such as reconnaissance and acquisition, tracking, and pointing systems, an image-based point-and-track algorithm is often used. Therefore, the ability to conduct high-speed and accurate imaging through a variety of fluid environments is required. More broadly speaking, image quality can be affected by both atmospheric optical turbulence and aero-optical effects. Aero-optical-induced distortions are resultant from either compressibility effects when speeds exceed Mach 0.3 or local changes in pressure associated with aerodynamic flow environments around an aircraft such as boundary layers (BL) or shear layers (SL).^{1,2} If a system is placed on a high-speed aircraft, the flow around the aircraft introduces additional optical distortions that ultimately limit the effectiveness of these systems. These aero-optical-induced effects are fundamentally different from the distortions imposed by atmospheric propagation. When a light or laser beam is transmitted through the atmosphere, the local total temperature variations are attributed with being the primary source of atmospheric distortions.³ This paper will focus solely on image degradation due to aero-optical-induced effects.

The Airborne Aero-Optics Laboratory (AAOL) was established to provide a subsonic⁴ and transonic⁵ in-flight testing platform where aero-optics experiments can be performed under real conditions. Recent work on AAOL-beam control (AAOL-BC) has both qualitatively and quantitatively described the wavefront aberrations imposed on an incoming laser beam through a variety of aero-optical environments around AAOL-BC.⁶ As an initially unperturbed laser beam is projected from a source, through an aero-optical environment to a target, the imposed distortions result in a larger than diffraction limited size spot in the far-field. Consequently, less intensity is focused on the target. Similarly, imaging a distant object through these same distortions will degrade the resultant image quality. Coupling the ability to quantify aero-optical

*Address all correspondence to Stanislav Gordeyev, sgordeye@nd.edu

distortions using wavefront measurements while simultaneously recording high-speed images enables the deleterious nature of imaging through these flow environments to be studied. For example, previous work⁷⁻⁹ has characterized the imaging environment associated with looking through an optical turret, and image distortions were computed using only wavefront data. In this study, in-flight imaging tests were performed looking through two fundamental aerodynamic flows, namely a BL and an SL. Both instantaneous wavefront and resultant image distortions were synchronously measured using two high-speed cameras to investigate the image degradation resultant from relevant flow features present in these fundamental aero-optical environments. To the authors' knowledge, it was the first time that both instantaneous wavefronts and resultant distorted images were simultaneously recorded in a realistic flight environment. In addition, the experimental setup and processing procedure for handling both image and wavefront flight data are presented.

2 Experimental Setup

AAOL-BC consists of two Falcon-10 aircraft flying in close formation $L \sim 60$ m apart. One of the aircraft is retrofitted with a target board design pattern on the aircraft window. This aircraft, otherwise known as the “source aircraft,” projects a 532-nm diverging laser beam, generated by a YAG:Nd laser, from a rectangular slit in the middle of the target board onto a custom-designed optical quality window mounted on the second aircraft. The second aircraft, known as the “laboratory aircraft,” is accommodated with an optical system to receive the incoming beam and to image the target board on the source aircraft. A custom-made BK-7 window, shown in Fig. 1(a), through which the laser beam is received and the target board is imaged, has a clear aperture of 0.30 m in diameter with a spatial rms wavefront error of less than $\lambda/10$. The window is mounted in an aluminum insert designed to minimize distortions to the attached BL as fluid convects from the aircraft fuselage over the window. Wavefront and high-speed images were collected through the BL of AAOL-BC at Mach numbers of 0.5, 0.6, and 0.7. In a separate experiment,⁶ the BL was studied using an array of pitot rakes in the location of the optical window. The results showed that the BL thickness was approximately $\delta = 4.5$ cm and was aero-optically similar to the canonical BL developed over a flat plate. More details about aerodynamic and aero-optical properties of the BL can be found in Ref. 6.

An SL was generated over the optical window by installing a porous fence 0.35 m upstream of the acquisition window on the laboratory aircraft, as seen in Fig. 1(b). Previous work illustrated the utility of porous fences as passive flow devices, in which an SL was created by slowing the flow downstream of the fence via turbulence-related total pressure losses.¹⁰ The fence has a semicircular shape with a radius of 0.152 m and is installed normal to the aircraft surface on a mounting bracket. The fence had a porosity coefficient, defined as the area of open holes in the fence divided by the total fence area, of 0.4.⁶ Wavefront and high-speed images were collected

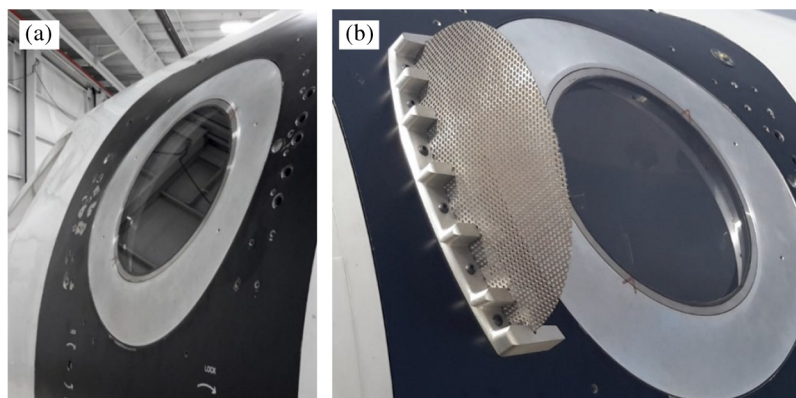


Fig. 1 (a) Flat window for BL tests. (b) Perforated plate installed in front of the flat window for SL studies.

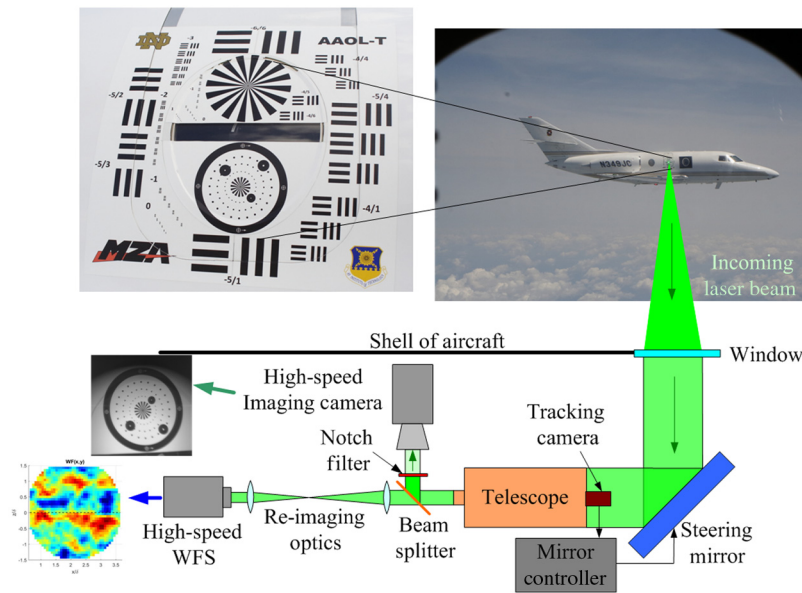


Fig. 2 The optical setup and acquisition system on the AAOL-BC.

through the SL environment generated around AAOL-BC at Mach numbers of 0.5, 0.6, and 0.7. The characteristic streamwise length for the SL was found to be $\Lambda = 0.13$ to 0.14 m, depending on the flight Mach number. More information about the statistics of the SL aero-optical distortions can be found in Ref. 6.

High speed images and instantaneous wavefronts were taken concurrently. The laboratory aircraft was equipped with a beam stabilizing system, reimaging optical components, a high-speed Shack–Hartmann wavefront sensor (SHWFS), and a high-speed imaging camera. The optical setup is shown in Fig. 2. The source aircraft flew slightly above the laboratory aircraft such that the incoming beam was roughly normal to the flat window on the laboratory aircraft. Both the laser system on the source aircraft and the acquisition system on the laboratory aircraft utilized independent tracking systems. The laser system must be tracking to aim the beam at the correct location on the laboratory plane, despite relative aircraft motion, mechanical vibration, and other system noise. The acquisition system on the laboratory aircraft used an image-based Fitts tracking algorithm to ensure that the incoming beam was stabilized through the optical train and that the high-speed camera focused on the appropriate target board location on the source aircraft. The incoming beam was stabilized using a computer-controlled proportional feedback system, which consisted of a tracking camera, a mirror controller, and a motorized Aerotech gimbal with a flat mirror 0.3048 m in diameter. The tracking camera on the laboratory aircraft collected images at 200 fps and computed relative image displacements in both the horizontal and vertical directions. Using these computed displacements, the mirror controller commanded motors on the gimbal to compensate for these angular differences.

After stabilization, the laser beam entered a Schmidt–Cassegrain telescope with an aperture diameter of $D = 0.2032$ m or aperture radius of $R = 0.1016$ m, a central obscuration 64 mm in diameter (or 31% obscuration by diameter), and a focal length of 2.035 m. A beam splitter then partitioned the received light between the SHWFS and the high-speed imaging camera. The portion of the beam directed toward the SHWFS was recollimated using a 200-mm focal length lens and was further contracted with a 250- and 200-mm lens pair, resulting in a collimated 16-mm diameter beam entering the sensor. The SHWFS used a Phantom v1611 high-speed camera with a pixel size of $28\ \mu\text{m}$ and a rectangular lenslet array mounted on it. The lenslet array has a spatial resolution of 50×50 subapertures with a 0.3 mm pitch and 38.2 mm focal length, allowing the wavefront imposed on the beam to be measured with high spatial accuracy. Wavefronts were acquired at 25 kHz and an exposure time of $0.4\ \mu\text{s}$ for 1.12 s, producing 28,000 frames per collection. For the portion of the beam directed toward the high-speed imaging

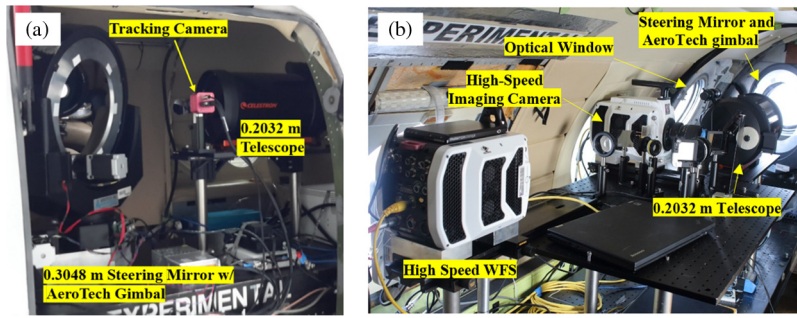


Fig. 3 Interior of laboratory aircraft of AAOL-BC from (a) the exit door and (b) the back of the optical table.

camera, a dichroic notch filter was placed in front of the imaging camera to attenuate the 532-nm wavelength to avoid possible damage to the imaging camera. A Phantom v1840 high-speed camera with a pixel size of $13.5 \mu\text{m}$ was used as the imaging camera, coupled with a Canon MP-E 65-mm $1\times$ magnification lens. Images were acquired at 8.1 kHz with an exposure time of $120 \mu\text{s}$. A trigger was set between the SHWFS and the high-speed imaging camera to ensure the same initiation time for data synchronization. Flight static temperatures, pressures, and Mach numbers were also recorded during the flight. Figure 3(a) shows the interior of the laboratory aircraft from the exit door where the optical window, seen in Fig. 1, is located. Figure 3(b) shows the rest of the laboratory aircraft configuration aft of the optical train.

The target board, imaged by the laboratory aircraft, can be seen in the top left of Fig. 2. Here, three different target board designs were employed. During the experiment, the target board was illuminated by the ambient sunlight. The black, horizontal, and vertical rectangle patterns were designed to match the USAF-1951 target board. A spoke pattern was also implemented on the target board directly above the rectangular slit out of which the laser source is projected. The utility of this design is that the spoke pattern offers a wide range of spatial frequencies. The last design pattern implemented below the rectangular slit consists of a series of dots, decreasing in size as they get closer to the center of the target pattern. The results discussed in this paper will focus on the resultant images taken of this dot pattern design.

3 Data Analysis

Time-resolved wavefronts, $W(x, y, t)$, were computed from the SHWFS images using in-house software. In this work, the streamwise direction will be denoted as the x -direction and the cross-stream direction will be denoted as the y -direction. Steady-lensing and instantaneous tip and tilt components were removed from every wavefront. The levels of aero-optical distortions were quantified by the time-averaged spatial root-mean-square (rms) of the wavefronts, denoted as $W_{\text{rms}} = \overline{W_{\text{rms}}(t)}$, where $W_{\text{rms}}(t) = \sqrt{\langle W(x, y, t)^2 \rangle_{\text{OverAperture}}}$, the angular brackets denote averaging over the aperture, and the overbar indicates time averaging.

The experimentally measured wavefronts were used to compute the instantaneous point spread functions (PSFs), denoted as

$$s(\theta_x, \theta_y, t) = \frac{\left| \int_{\text{Aperture}} \sqrt{I_0(x', y')} \exp\left\{ \frac{2\pi i}{\lambda} [W(x', y', t) - (x' \cdot \theta_x + y' \cdot \theta_y)] \right\} dx' dy' \right|^2}{\left| \int_{\text{Aperture}} \sqrt{I_0(x', y')} dx' dy' \right|^2}. \quad (1)$$

Here, I_0 is the near-field intensity (assumed to be a top-hat function), L is the distance to the target, and $(\theta_x, \theta_y) = \frac{(x, y)}{L}$ are the angular coordinates. PSFs were computed via numerical integration over a discrete number of aperture points (x', y') .

As mentioned, the target board was illuminated by the sunlight, with the wavelength corresponding to the maximum radiation intensity of the solar spectrum of $0.5 \mu\text{m}$. However,

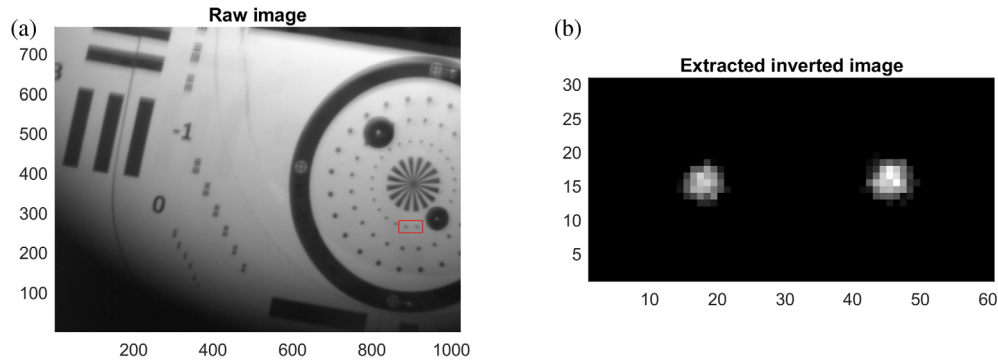


Fig. 4 (a) Example of the original image, collected in flight. The region of interest is indicated by a red box. (b) Extracted and inverted region of interest used for the analysis.

images were recorded using a Phantom camera, which has the responsivity peak near $0.625 \mu\text{m}$. The product of the solar spectrum and the camera responsivity curve was computed (not shown), and the peak wavelength was found to be near $0.55 \mu\text{m}$. Based on this value, the reference wavelength was chosen to be $\lambda = 0.55 \mu\text{m}$.

A representative example of a collected image is shown in Fig. 4(a). Since the target board was placed over the curved aircraft window, only part of the image was in focus. A region of the in-focus portion of the image, as indicated by a red box in Fig. 4(a), was extracted from every frame. This region was 30×60 pixels in size and included two 1-mm diameter dots, separated by 9 mm center to center on the target board. The extracted image, $K(x, y, t)$, was corrected for brightness and inverted such that the dots would have large positive intensity values and the background was near zero intensity. An example of the processed image used for further analysis is shown in Fig. 4(b). A reference ground image was also collected with both aircraft positioned on the tarmac at the same separation distance of $L = 60$ m. Later it will be referred to as the ground image, K_{Ground} . The ground image was collected during neutral atmospheric conditions near sunset, when the air turbulence near the ground was minimal and the ground image can be treated as an undistorted reference image of the dots.

From Fig. 4(b), the distance between the dots is about 30 pixels, giving the relationship between the target board space, later called the object plane (in mm), and image space (in pixels) as $\sim 0.3 \text{ mm/pixel}$. The radius of the diffraction-limited Airy disk, R_{Airy} , defined as the radius to the first intensity minimum in the object plane, is $R_{\text{Airy}} = 1.22 \frac{\lambda L}{D} = 0.19 \text{ mm}$. Using this value, the pixel size in the object plane was computed to be $0.3 \text{ mm} = 1.58 R_{\text{Airy}}$. Having a relatively large pixel size, comparable with the Airy disk, is prohibitive for computing Strehl ratio directly from the images. However, power-in-bucket (PIB) values can still be computed inside the square area with a side length of $1.58 R_{\text{Airy}}$ from the image data.

Using the collected flight images, $K(x, y, t)$, instantaneous time traces of $\text{PIB}(t)$ were extracted as instantaneous pixel intensities at the center of each dot for different Mach numbers and flow cases over the window. PIBs from both dots were averaged together to reduce experimental noise. As a reference, the ground image, K_{Ground} , was used to extract $\text{PIB}_{\text{NoFlow}}$, and the PIB ratios, $\text{PIB}(t)/\text{PIB}_{\text{NoFlow}}$, were analyzed.

To compare with the PIB ratios directly extracted from the images, $\text{PIB}(t)$ were also computed from instantaneous PSFs using Eq. (1), via integration over the pixel area in the object plane,

$$\text{PIB}(t) = \int_{-0.79R_{\text{Airy}}}^{0.79R_{\text{Airy}}} \int_{-0.79R_{\text{Airy}}}^{0.79R_{\text{Airy}}} s(x, y, t) dx dy. \quad (2)$$

A similar equation, but without optical distortions [that is, with $W(x, y) = 0$ in Eq. (1)], was used to compute $\text{PIB}_{\text{NoFlow}}$. Note that PIB was computed over a square area, giving “ensquared” energy, rather than the more traditional “encircled” energy.

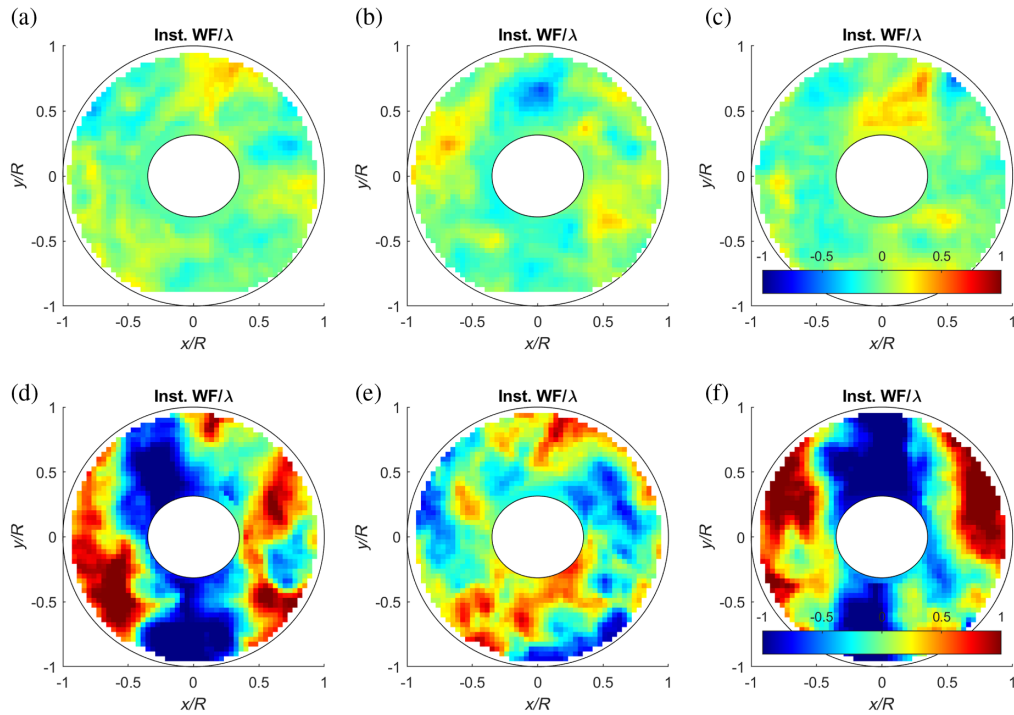


Fig. 5 Representative instantaneous wavefronts, in waves, for (a)–(c) the BL case, $M = 0.7$ and (d)–(f) the SL case, $M = 0.7$. Spatial coordinates are normalized by the aperture radius, R .

4 Results

4.1 Analysis of Apertured Data

The representative wavefronts (in waves) collected through the aircraft BL at Mach number $M = 0.7$ are presented in Figs. 5(a)–5(c). The distortions imposed by the BL are fairly small even at the highest Mach number of 0.7, with less than half a wave peak-to-valley. The SL generates a much stronger aero-optical environment and the distortions increase with increasing Mach number. An example of representative SL wavefronts for $M = 0.7$ are provided in Figs. 5(d)–5(f). Here, strong pseudoperiodic structures in the streamwise x direction, elongated in the cross-stream y direction are observed, with associated peak-to-valley values that exceed two waves. These aero-optical distortions are created by convecting vortical structures formed in the SL.¹¹ The W_{rms} values calculated for each test case are also presented in Table 1.

The SL cases clearly represent the scenarios of the most detrimental flow-field-induced aberrations, with associated distortions of $W_{\text{rms}}/\lambda > 0.3$ and significant image blurring. Conversely, the BL environments represent the more aero-optically benign cases. The BL over the aircraft window creates small, $<0.15\lambda$ distortions, and the resultant images are expected to be

Table 1 Values of aero-optical distortions for different flows cases and Mach numbers.

Flow and Mach number	W_{rms} (μm)	W_{rms}/λ
BL, $M = 0.5$	0.0552	0.10
BL, $M = 0.6$	0.0711	0.13
BL, $M = 0.7$	0.0816	0.15
SL, $M = 0.6$	0.172	0.31
SL, $M = 0.7$	0.249	0.45

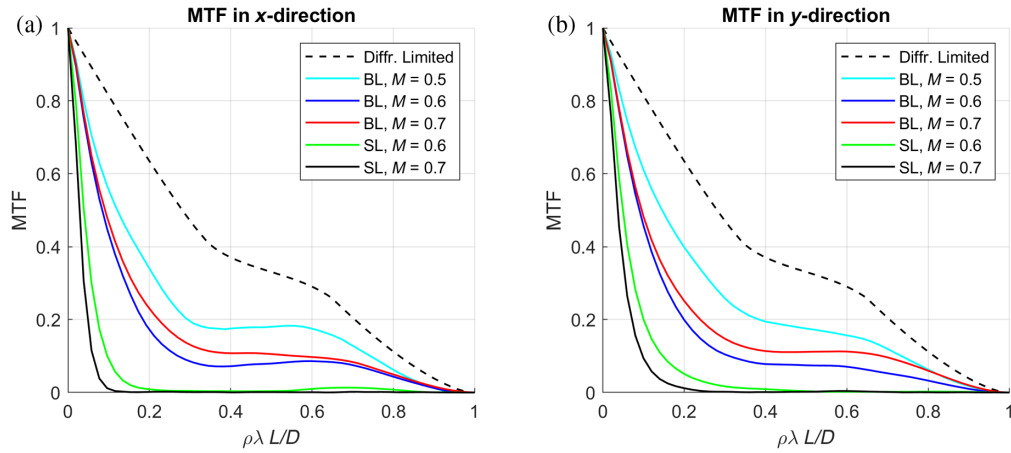


Fig. 6 Time-averaged MTFs, computed from the wavefronts in the (a) x direction and (b) y direction for both the BL and SL at different Mach numbers.

comparatively sharp. One way to demonstrate this is to compute time-averaged modulation transfer functions (MTFs) from the wavefront data. The resultant MTFs in both the x - and y directions for the BL case and the SL case at varying Mach numbers are shown in Fig. 6. The diffraction-limited MTF for the circular aperture with the circular obscuration is also presented in Fig. 6 as a dashed line for comparison. For the case of the BL, the MTFs are close to the diffraction-limited case. MTFs for the SL case show significant degradation, with more distortions in the streamwise direction compared with the cross-stream direction. This asymmetry effect will be discussed in more detail later in this paper.

Another way to demonstrate the asymmetry in image blurring is to compute time-averaged PSFs using Eq. (1). The results for the BL case are shown in Fig. 7, and PSFs for the SL case are presented in Fig. 8. Slices of the time-averaged PSFs for all cases in the streamwise x direction and the cross-stream y direction, along with the diffraction-limited (no distortion) PSF for comparison, are shown in Fig. 9. For the case of the less aberrating BL, PSFs in Figs. 7 and 9 do not show significant asymmetry and are close to the diffraction-limited PSF. In the case of the strongly aberrating SL, see Figs. 8 and 9, PSFs are clearly more spread in the streamwise direction compared with the cross-stream direction. In addition to the main peak, two side lobes appear in PSF for $M = 0.6$, see Figs. 8(a) and 9(a). Side lobes in the PSF usually indicate periodicity in the corresponding wavefronts. This observation is consistent with the presence of pseudoperiodic structures in the streamwise direction in the SL, as seen in Figs. 5(d) and 5(f).

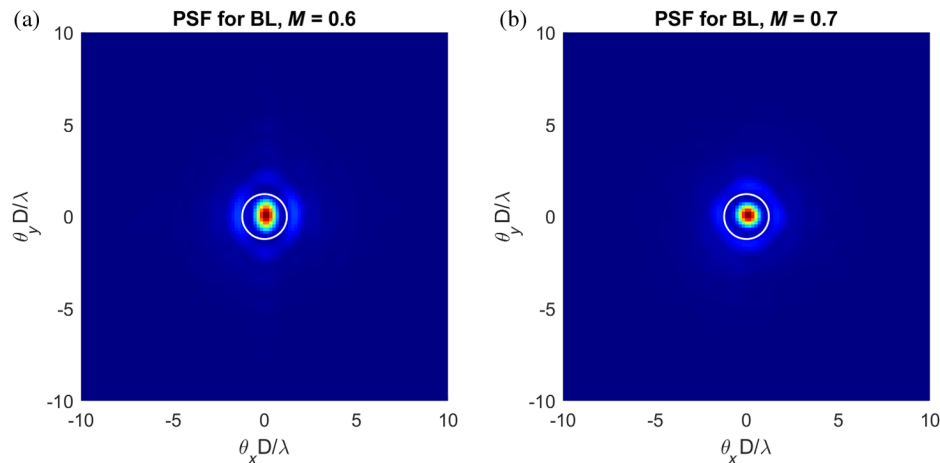


Fig. 7 Time-averaged PSFs, computed using the wavefronts, Eq. (1), for the BL case for flight Mach number of (a) $M = 0.6$ and (b) $M = 0.7$. Airy disk is indicated by a white circle.

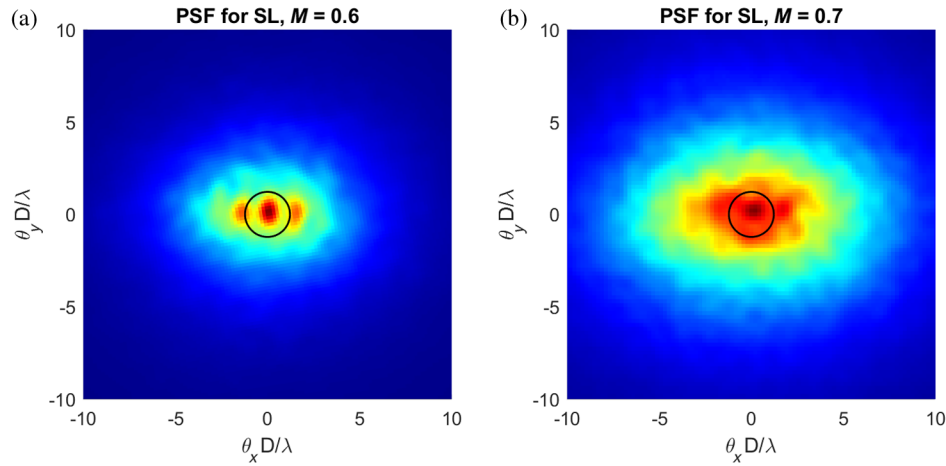


Fig. 8 Time-averaged PSFs, computed using the wavefronts, Eq. (1), for the SL case for flight Mach number of (a) $M = 0.6$ and (b) $M = 0.7$. Airy disk is indicated by a black circle.

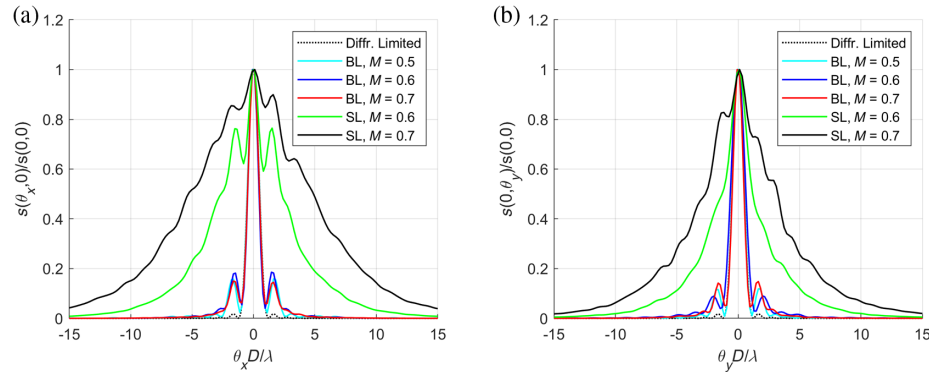


Fig. 9 Slices of time-averaged PSFs, computed using the wavefronts, Eq. (1), along the (a) x direction and (b) y direction, for all Mach numbers and flow cases.

To investigate the relationship between wavefront aberrations and image blurriness, instantaneous PIB ratios, $\text{PIB}(t)/\text{PIB}_{\text{NoFlow}}$, were extracted from the flight images (as discussed) for different flow cases. The results are presented in Fig. 10 as thick blue lines for the BL at $M = 0.7$ and for the SL at $M = 0.6$ and 0.7 . PIB ratios were also computed from instantaneous wavefronts using Eqs. (1) and (2) and are plotted in Fig. 10 as thin red lines for comparison.

For all flow cases, the agreement between the extracted and the computed PIB ratios is good, with both PIB ratios generally going up and down in concert. This confirms that the aero-optical distortions created by the turbulent flow are the main cause of the instantaneous image blurring. The observed small differences between the extracted and the computed PIB ratios are expected and are due to several factors. One of them is an associated numerical error in the discrete approximation of PSFs in Eq. (1). In addition, PSFs were computed using an assumption of a single wavelength of $\lambda = 0.55 \mu\text{m}$, while the collected images were lit by sunlight, which has a continuous wavelength range.

For the BL case, see Fig. 10(a), PIB ratios are high (about 0.7), as expected for the less optically aberrating flow. This observation is consistent with the analysis of MTFs and PSFs as discussed. When the flow becomes more optically distorted in the presence of the SL, PIB ratios expectedly drop to lower values, as seen in Figs. 10(b) and 10(c). Again, this agrees with the analysis of MTFs and PSFs presented earlier. For the $M = 0.6$ case, given in Fig. 10(b), both PIB ratios show increased relative temporal variations between the values of 0.15 and 0.35. When the Mach number is increased to 0.7, Fig. 10(c), the PIB ratios become even lower, with a significant temporal variation between 0.05 and 0.3.

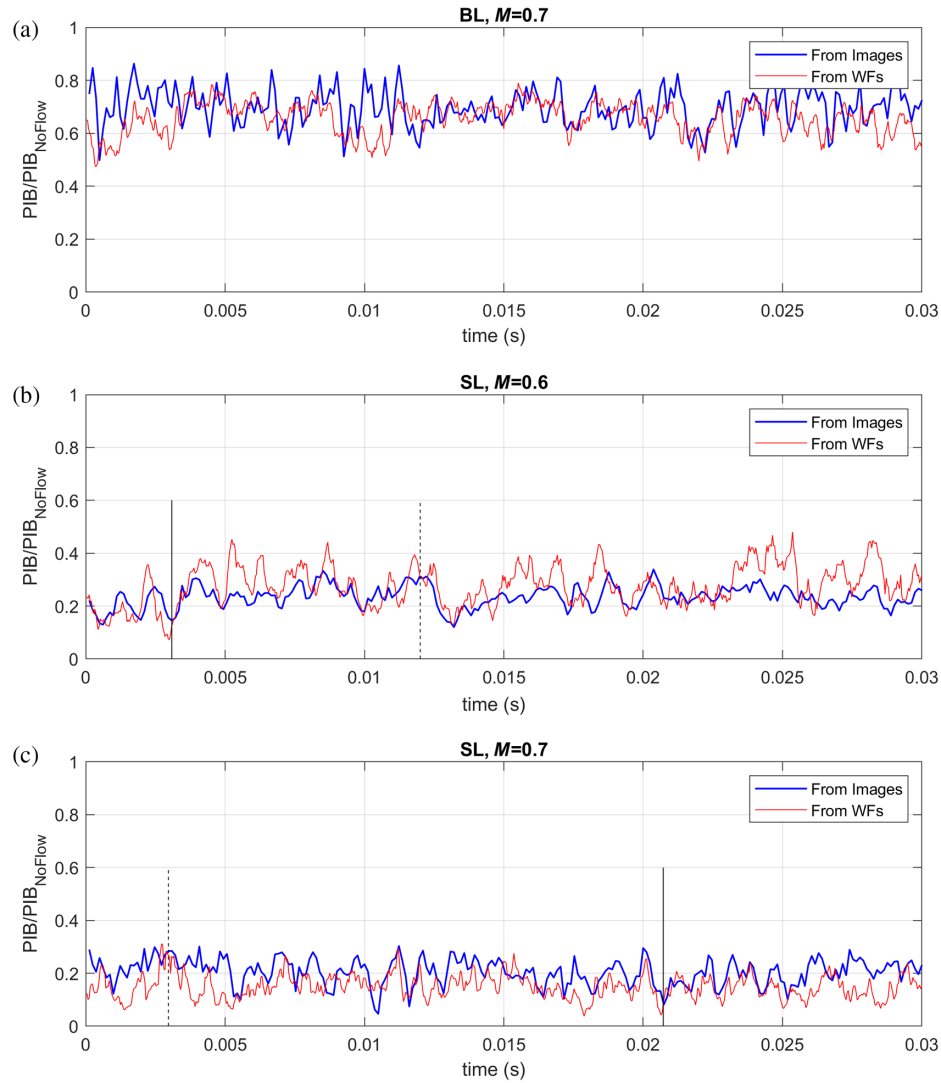


Fig. 10 Instantaneous PIB, normalized by PIB_{NoFlow} , extracted from images (blue thick lines) and computed from wavefronts, using Eq. (2) (red thin lines) for (a) the BL case, $M = 0.7$, (b) the SL case, $M = 0.6$, and (c) the SL case, $M = 0.7$. Solid and dashed vertical black lines in (b) and (c) indicate selected time instances for additional studies presented in Figs. 12 and 13.

Another way to quantify the relation between the instantaneous PIB ratios and the underlying flow features is to compute the power spectral density (PSD) of PIB ratios. Results for the BL case for $M = 0.7$ and the SL case for $M = 0.7$ are shown in Fig. 11. PSD were calculated using pwelch-function in MATLAB with 50% overlap. Since the SL has a range of preferred frequencies, the PSD has a narrow band of about 900 Hz, corresponding to the main temporal frequency of the large-scale structures. The PSD for the BL has a wide range of frequencies, characteristic of turbulent BLs.

PIB ratios for the SL cases in Figs. 10(b) and 10(c) show significant temporal variations. If the PIB ratio is small, more image blurring is evident. When the PIB ratio is higher, less image blurriness is expected. As observed in the representative wavefronts in Figs. 5(d)–5(f), the SL flow is dominated by the large, pseudoperiodic structures in the streamwise direction, which are nearly uniform in the cross-stream y direction. As aberrating wavefronts show spatial asymmetry, the images are also expected to demonstrate the asymmetric blurriness. To further investigate which specific aero-optical features cause this asymmetric blurriness, time instances in which PIB ratios were small, indicated by solid vertical lines in Figs. 10(b) and 10(c), were selected. Similarly, time instances with large PIB ratios, indicated by dashed vertical lines in Figs. 10(b)

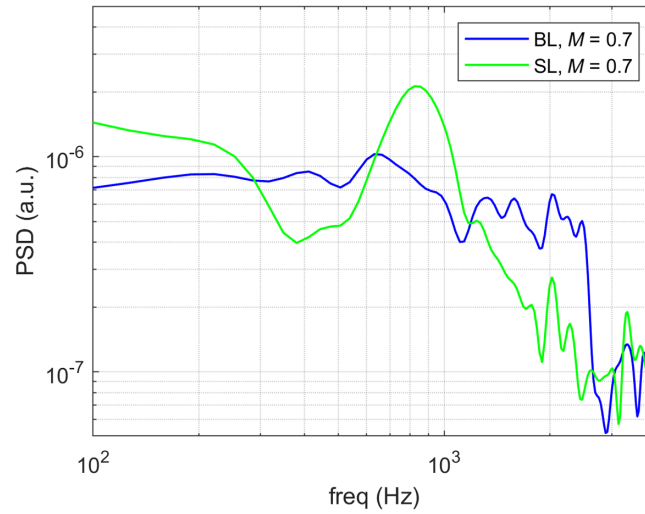


Fig. 11 PSDs of instantaneous PIB ratios, for the BL case, $M = 0.7$ and the SL case, $M = 0.7$.

and 10(c), were also selected. For these time instances, the measured dot image, K , was compared with the simulated blurred dot image. The simulated blurred image was computed by convolving the pixelated model of the 1 mm in diameter dot, K_{Dot} , with the instantaneous PSF, $K_{\text{Dot}}(x, t) * s(x, y, t)$.

For the selected times, the instantaneous wavefronts, the corresponding simulated dot images, and the extracted dot images are shown in Fig. 12 for $M = 0.6$ and Fig. 13 for $M = 0.7$. For $M = 0.6$, see Figs. 12(a)–12(c), when the PIB ratio is low (at $t = 0.003$ s) both the simulated, Fig. 12(b), and experimental, Fig. 12(c), images clearly show that the dot image is distorted predominantly in the streamwise direction. The similarity between the computed dot shape and

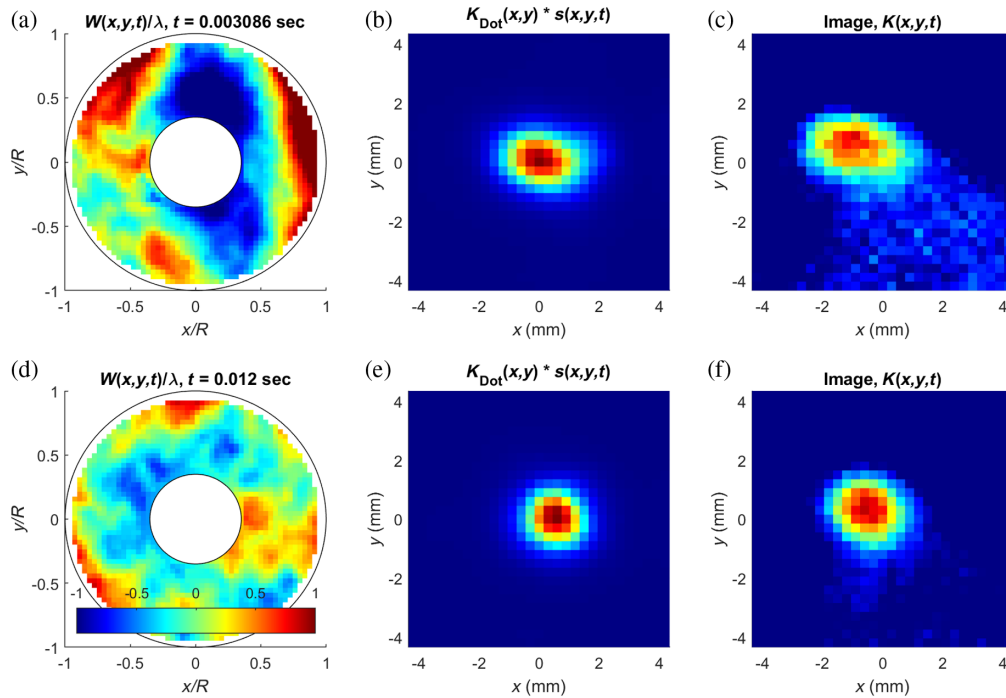


Fig. 12 (a), (d) The instantaneous wavefronts, (b), (e) the simulated dot images, and (c), (f) the measured dot images for selected times of (a)–(c) $t = 0.003$ s, indicated by a vertical solid line in Fig. 10(b), and (d)–(f) $t = 0.012$ s, indicated by a vertical dashed black line in Fig. 10(b) for the SL at $M = 0.6$.

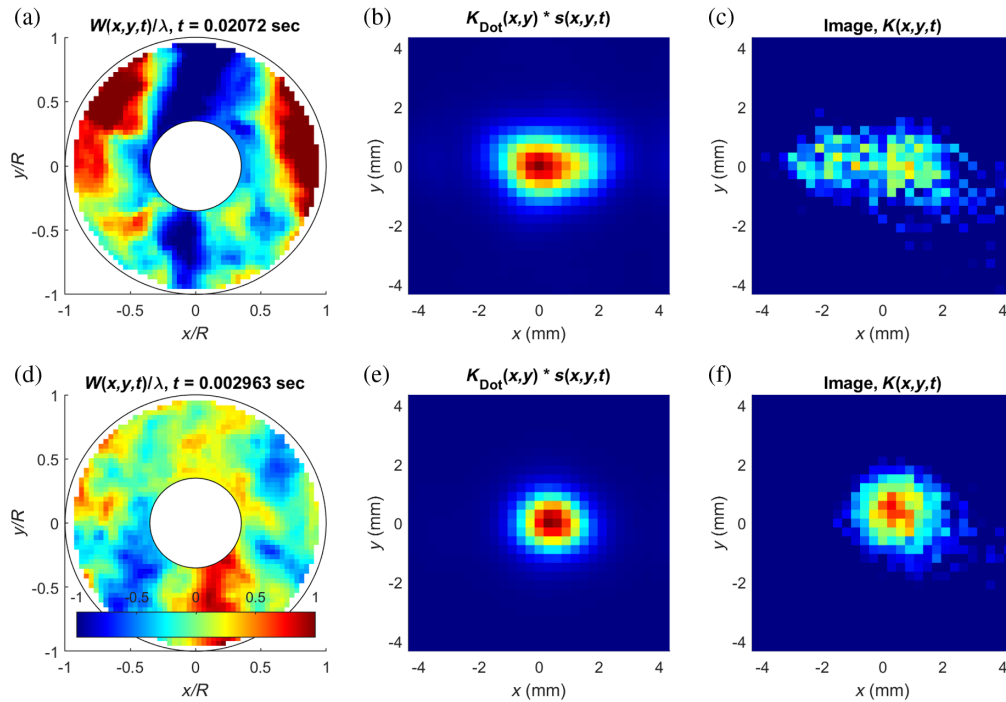


Fig. 13 (a), (d) The instantaneous wavefronts, (b), (e) the computed dot images, and (c), (f) the measured dot images for selected times of (a)–(c) $t = 0.021$ s, indicated by a vertical solid line in Fig. 10(b), and (d)–(f) $t = 0.003$ s, indicated by a vertical dashed black line in Fig. 10(c) for the SL at $M = 0.7$.

the experimentally extracted one is clear, indicating that the SL was the most significant source of optical distortion, while other sources of optical distortions, such as nonideal optical components and mechanical vibrations of the optical components, were sufficiently small. The corresponding wavefront, shown in Fig. 12(a), shows the presence of strong optical distortions, with peak-to-valley values close to two waves and elongated in the cross-stream y direction. However, when the PIB ratio is high at $t = 0.012$ s, see Figs. 12(d)–12(f), the wavefront shows relatively weak aero-optical distortions with no observable spatial organization. Consequently, both the simulated, shown in Fig. 12(e), and the measured, see Fig. 12(f), dot images are blurred by approximately the same amount in both directions. Again, the computed dot shape and size is very close to the experimentally extracted one.

The same asymmetric large amplitude wavefronts and dot images, elongated in the streamwise direction, for a low PIB ratio at $t = 0.021$ s were also observed at a higher Mach number of 0.7, see Figs. 13(a)–13(c). The extracted dot image shows large streamwise blurriness. Compared with the computed dot image, the extracted image is noisy as the PIB ratio is very low (about 0.1 at this instance). Again, when the PIB ratio was high at $t = 0.003$ s, the wavefront was less aberrating and the dots were blurred less and appear to have a symmetric shape, see Figs. 13(d)–13(f). Thus, the large, spatially organized structures present in the SL are the most significant source of optical distortions, blurring the dot images predominantly in the streamwise direction.

Both the wavefront and the image collection systems are affected by various corrupting effects, such as nonideal optical components, mechanical vibrations, and the relative motion of the aircraft. For the wavefronts, these effects can be easily removed in postprocessing analysis. All of the mentioned corrupting effects will also degrade the quality of the image measurements. It is possible to apply various algorithms, such as blind image deconvolution or phase retrieval to remove aero-optical degradation of the images during the postprocess stage, but they are typically computationally intensive and time consuming. A good agreement between the extracted and the computed images demonstrates that instead of developing expensive optical setups to directly measure the instantaneous aero-optical image distortions in-flight, it is possible to

compute the images from the properly processed wavefronts. In our opinion, it provides a new possibility for studying aero-optical-related image distortions and potentially mitigating these distortions in image-based tracking systems.

4.2 Time-Averaged or Long-Exposure PSFs for any Apertures

In many cases, the exposure time for imaging cameras is larger than the characteristic time scales of the aberrating flow structures, which are on the order of Λ/U_∞ , where U_∞ is the aircraft speed and Λ is a characteristic streamwise length scale. Consequently, the instantaneous blurring effect from many convecting flow structures will be averaged out. In this case, it is possible to compute the resultant long exposure PSF if the wavefront statistics are known. For incoherent imaging, the PSF can be found as a spatial Fourier transform of the optical transfer function, $H(\mathbf{k})$,¹²

$$\text{PSF}(\mathbf{x}) = \int H(\mathbf{k}) \exp(2\pi i \mathbf{k} \cdot \mathbf{x}) d\mathbf{k}, \quad (3)$$

where $\mathbf{k} = (k_x, k_y)$ is the two-dimensional spatial frequency. In turn, the optical transfer function of the overall optical system is a product of a transfer function of fixed optics, $H_O(\mathbf{k})$, and a corresponding long-exposure optical transfer function of the aberrating flow, $H_{LE}(\mathbf{k})$,¹²

$$H(\mathbf{k}) = H_{LE}(\mathbf{k})H_O(\mathbf{k}). \quad (4)$$

For instance, for a circular aperture, H_O is given as¹²

$$H_O(\mathbf{k}) = \begin{cases} \frac{2}{\pi} \left[\cos^{-1}(z) - z\sqrt{1-z^2} \right], & z \leq 1 \\ 0, & z > 1 \end{cases}, \quad (5)$$

where $z = |\mathbf{k}| \lambda L / D$ and L is the distance to the target.

For apertures larger than a characteristic flow length scale, spatial distributions of the wavefronts for both the BLs^{13,14} and the SLs¹⁵ can be reasonably approximated as Gaussian. For a plane wave propagating through a spatially Gaussian random field, it is straightforward to show¹² that $H_{LE}(\mathbf{k})$ can be computed using a phase structure function, $D(\Delta\mathbf{x})$, as

$$H_{LE}(\mathbf{k}) = \exp \left[-\frac{1}{2} D(\lambda L \mathbf{k}) \right], \quad (6)$$

where $D(\Delta\mathbf{x}) = 2 \left(\frac{2\pi W_{\text{rms}}}{\lambda} \right)^2 [1 - \rho(\Delta\mathbf{x})]$ and $\Delta\mathbf{x} = (\Delta x, \Delta y)$. The normalized spatial autocorrelation function, $\rho(\Delta x, \Delta y)$, can be computed from the wavefronts as

$$\rho(\Delta x, \Delta y) = R(\Delta x, \Delta y) / R(0), \quad R(\Delta x, \Delta y) = \overline{\int W(x, y, t) W(x - \Delta x, y - \Delta y, t) dx dy},$$

where the overbar denotes the time averaging. From Eq. (6), it follows that the phase structure function is proportional to $(2\pi W_{\text{rms}}/\lambda)^2$,² and therefore, for large W_{rms}/λ -ratios, the resultant image distortions will be severe.

Since the wavefronts were collected over the finite-size aperture ($D = 0.2032$ m), which is comparable in length scale to the typical SL flow structure ($\Lambda = 0.13$ m), significant tip/tilt is present in the wavefronts. Recall that environmental mechanical corruption also introduces tip/tilt into the wavefront data. Therefore, overall tip/tilt, both aero-optical and mechanical, was removed from the wavefronts. This tip/tilt removal will result in modification of the spatial statistics of the residual wavefronts, the so-called aperture effects.^{16–18} Since aero-optical tip/tilt is removed from the wavefronts, important information about the spatial scales larger than the aperture size is also removed. Furthermore, even correlations for spatial separations smaller than the aperture diameter will be modified.¹⁶

One way to reconstruct a correct spatial autocorrelation is to recognize that, since the wavefronts are primarily convective in nature, it is possible to recover the correct wavefront spatial statistics in the streamwise direction by extending the wavefronts to any aperture length and

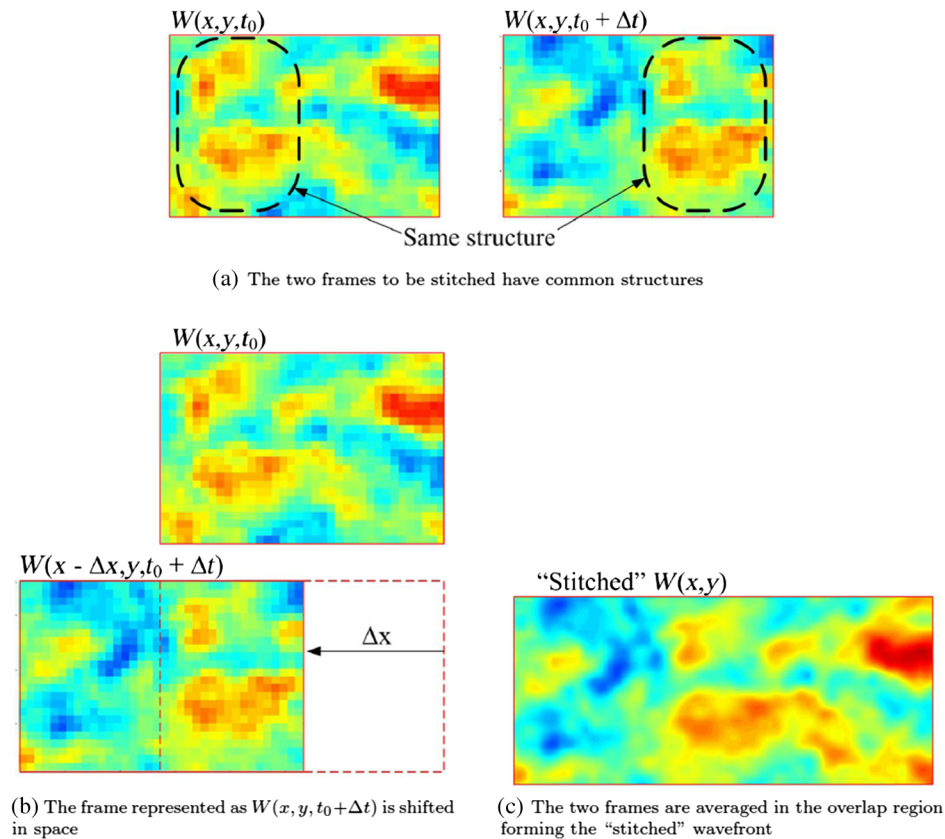


Fig. 14 “Stitching” of two frames $W(x; y; t_0)$ and $W(x; y; t_0 + \Delta t)$. Reproduced with permission from Ref. 19.

re-introducing the removed tip/tilt component using the stitching method.^{14,19} Briefly, the stitching method relies on Taylor’s Frozen Field Hypothesis between wavefronts collected in adjacent times. If the underlying structure does not change or evolve between adjacent frames and is instead primarily convective or simply shifts downstream, the distorting structures should be spatially the same but located at different, further downstream locations. The region of commonality between two consecutive frames is referred to as the overlapping region, see Fig. 14(a). By shifting the wavefront, taken at a later time, by $\Delta x = -U_C \Delta t$ (U_C is the convective speed), as shown in Fig. 14(b), and adding piston and tip/tilt components to the shifted wavefront until the least-square error between the wavefronts in the overlapping region at two adjacent times is minimized, it is possible to recover only the aero-optical piston and tip/tilt components, which were originally removed from the wavefronts. Recall again that piston, tip, and tilt are traditionally removed in typical wavefront processing as mechanical contamination is coupled with turbulence-induced tip and tilt. This stitching procedure allows for the turbulence-induced contribution of these quantities to be reintroduced, free of the inconvenient mechanical contamination, which is irrelevant for this analysis. This stitching method is repeated among adjacent frames to get a long streamwise strip of the wavefronts, as schematically shown in Fig. 14(c). Note that the stitching method also fills the center obscuration in the wavefronts.

Using the stitching method, long strips of the wavefronts were computed for both the SL and the BL cases. The wavefronts were broken into 100 blocks of no-overlapping wavefronts 1.4 m long in the streamwise direction, and unbiased estimates of spatial autocorrelations were computed. The normalized spatial autocorrelation for the SL case at $M = 0.6$ is shown in Fig. 15. A pseudoperiodic nature of the SL in the streamwise direction is clearly visible by the alternating regions of positive and negative correlation in the streamwise direction. Using the stitching method, it was now possible to correctly recover the autocorrelation function at large separations. In addition, the correlation is elongated in the cross-stream direction, indicating the presence of a pseudo one-dimensional large-scale structure. The normalized spatial autocorrelation functions

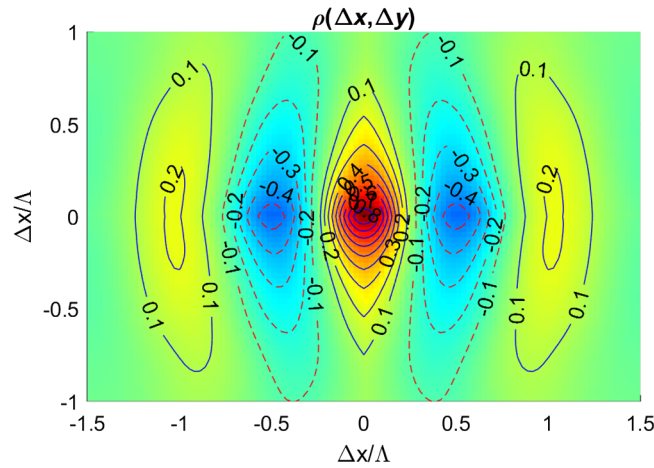


Fig. 15 Normalized unbiased spatial autocorrelation function, $\rho(\Delta x, \Delta y)$, for the SL case at $M = 0.6$, computed using the stitching method. Spatial coordinates are normalized by the SL streamwise structure length, $\Lambda = 0.135$ m.

for $M = 0.5$ and $M = 0.7$ are very similar to the one at $M = 0.6$ and therefore are not presented here.

Using the experimentally extracted spatial autocorrelation function from Fig. 15, the time-averaged or long exposure PSFs for the SL case can be computed for a circular aperture using Eqs. (3)–(6) for any D and W_{rms}/λ -ratio. Long exposure PSFs, computed for the current aperture diameter of $D = 0.2032$ m, using experimentally measured W_{rms} values at different Mach numbers, are shown in Fig. 16. For a Mach number of 0.5, the W_{rms}/λ -ratio is small and the PSF, shown in Fig. 16(a), is close to the diffraction-limited one. At $M = 0.6$, see Fig. 16(b), the W_{rms}/λ goes up, and the PSF shows increased distortions primarily in the streamwise direction, with two lobes developing on both sides of the main peak. Overall, the time-averaged PSF is similar to the one computed directly from the wavefronts, presented in Fig. 8(a), although the PSF in Fig. 8(a) is more elongated in the streamwise direction and has stronger side lobes. At the highest Mach number of 0.7, presented in Fig. 16(c), the distortions are significant enough to blur the image in both directions. Again, the time-averaged PSF, while narrower in the streamwise direction, is similar to the computed one in Fig. 8(b). Possible reasons for these small differences in PSFs in Figs. 16(b) and 16(c) and in Fig. 8 include the assumption of Gaussian-distributed wavefronts and different aperture shapes (the circular one in Fig. 16 and the circular one with the central obscuration in Fig. 8).

The described procedure allows one to compute time-averaged PSFs for any aperture diameter. For instance, if the aperture size is increased to $D = 0.4$ m, correlations at larger spatial separations will also affect PSFs, resulting in more spatially extended PSFs, relative to the

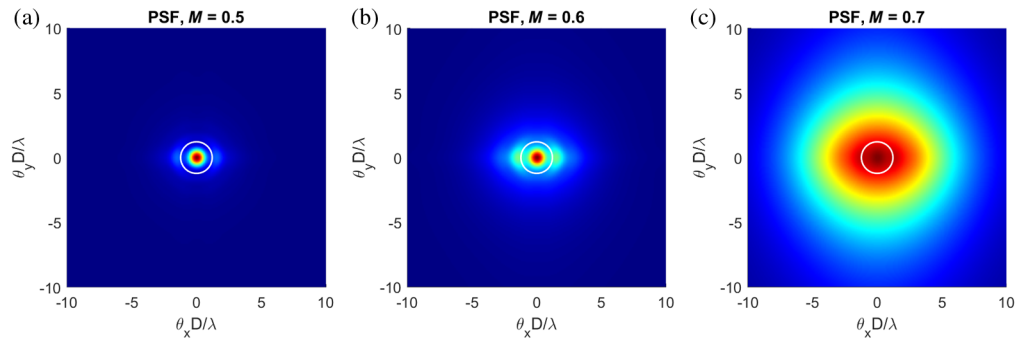


Fig. 16 Long exposure PSFs for the SL case, computed for a circular aperture with $D = 0.2032$ m and experimentally measured W_{rms} values at Mach numbers of (a) $M = 0.5$, (b) $M = 0.6$, and (c) $M = 0.7$. $\lambda = 0.55$ μm . Airy disk is indicated by a white circle.

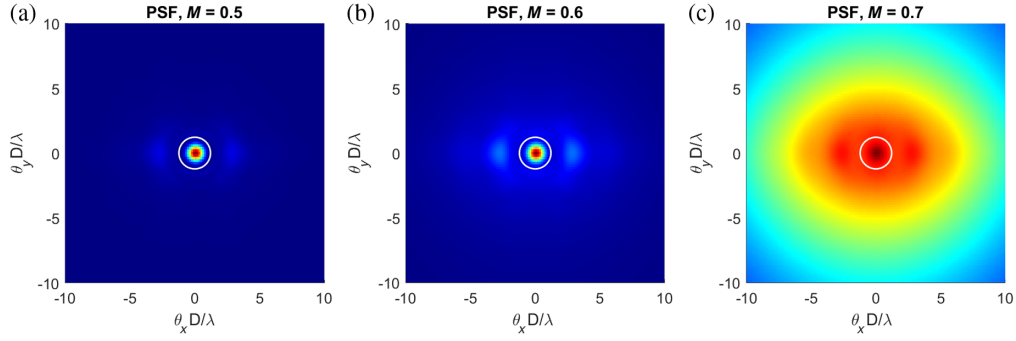


Fig. 17 Long exposure PSFs for the SL case, computed for a circular aperture with $D = 0.4$ m and experimentally measured W_{rms} values at Mach numbers of (a) $M = 0.5$, (b) $M = 0.6$, and (c) $M = 0.7$. $\lambda = 0.55 \mu\text{m}$. Airy disk is indicated by a white circle.

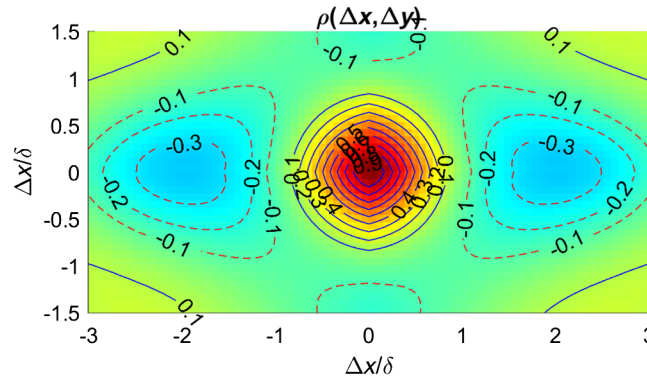


Fig. 18 Normalized unbiased spatial auto-correlation function, $\rho(\Delta x, \Delta y)$, for the BL case at $M = 0.7$, computed using the stitching method. Spatial coordinates are normalized by the BL thickness, δ .

diffraction-limited PSF. The computed time-averaged PSFs for the larger aperture at different Mach numbers are presented in Fig. 17 and indeed show larger relative streamwise blurriness at all Mach numbers, with the fainter side lobes appearing to be farther apart from the main peak. In fact, the angular separation of the side lobes depends only on the Λ/λ -ratio. Therefore, this ratio is the same as for $D = 0.2032$ m, but the far-field angles in Fig. 17 are multiplied by the larger D .

The normalized spatial autocorrelation function for the BL case at $M = 0.7$ is shown in Fig. 18. The spatial coordinates are normalized by the local BL thickness, δ . The BL structure does also show some periodicity in the streamwise direction, although with smaller values of negative autocorrelations of about -0.3 at $(\Delta x/\delta, \Delta y/\delta) = (\pm 2, 0)$. In contrast, the normalized spatial autocorrelation function for the SL case, shown in Fig. 15, has negative values of almost -0.6 at $(\Delta x/\Lambda, \Delta y/\Lambda) = (\pm 1, 0)$. Defining a BL correlation length as the distance between the adjacent negative peaks, the correlation length of the BL wavefronts was found to be about four BL thicknesses. The normalized autocorrelation function is very similar to the ones computed in numerical simulations of the aero-optical effects of the BL²⁰ and extracted from wind tunnel measurements.¹⁶

For the BL case, the values of W_{rms}/λ are less than 0.2, see Table 1, and the resultant PSFs are expected to be close to the diffraction-limited ones. Figure 19 presents PSFs, computed using the spatial autocorrelation function for the BL at $M = 0.5, 0.6$, and 0.7 . As expected, the PSFs have a diffraction-limited size. As in the SL case, the computed PSFs are similar to the ones presented in Fig. 7.

The outlined procedure, presented by Eqs. (3)–(6), can be easily extended to any aperture shape and size by properly choosing the transfer function of fixed optics, $H_O(\mathbf{k})$, in Eq. (5).

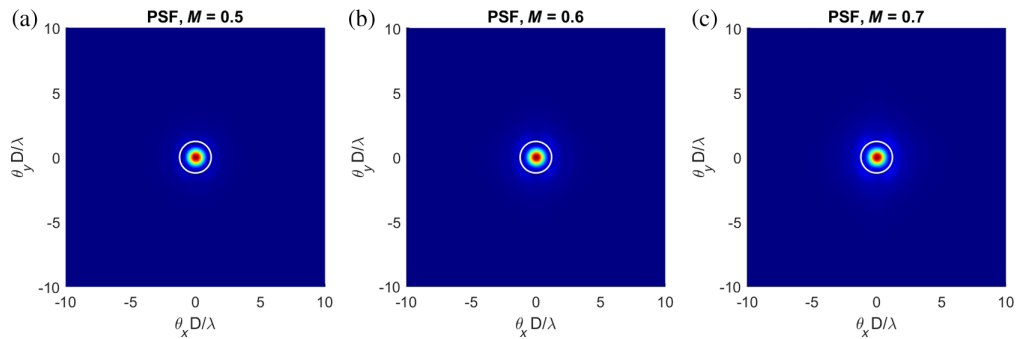


Fig. 19 Long exposure PSFs for the BL case, computed for a circular aperture with $D = 0.2$ m and experimentally measured W_{rms} values at Mach numbers of (a) $M = 0.5$, (b) $M = 0.6$, and (c) $M = 0.7$. $\lambda = 0.55$ μm . Airy disk is indicated by a white circle.

5 Conclusions

AAOL-BC was employed to acquire in-flight simultaneous wavefront and image data through two different fundamental aero-optical environments, a BL and an SL. Relationships between relevant flow structures and consequent image blurring were identified and further investigated. The BL environment did not impose appreciable distortions on the imaging results, and these scenarios were essentially diffraction limited. Conversely, the characteristic large-scale vortical structures indicative of SL environments did impose significant image degradation, especially in the streamwise direction. Using wavefront data, both the MTFs and PSFs for each test case were calculated and used to quantify these distortions. Also, PIB ratios were extracted from the image data and compared with the ratios computed from the wavefronts data. These ratios were found to correlate well with each other. It was found that when large-scale SL structures were present over the window, it resulted in a drop in PIB ratios and the images were distorted predominantly in the streamwise direction. When no organized optical structure was present over the window, it resulted in large values of PIB ratios and axisymmetric image blurring. This confirms that the convecting vortical SL large-scale structures are attributed with markedly increasing image blurring seen in the streamwise direction. It was also shown that knowing the spatial autocorrelation statistics of the aero-optical distortions allows long-exposure PSFs to be computed for an arbitrary aperture shape and size.

To correctly measure PSFs, expensive diffraction-limited optical setups are typically required. In this study, it was shown that a good agreement exists between directly measured distorted images and the images computed using properly processed wavefronts. Therefore, aero-optical-related image distortions can be investigated by measuring instantaneous wavefronts alone. Usually, experimental setups designed to collect wavefronts do not require expensive optics, and most of the corrupting effects, such as steady-lensing and mechanical vibrations, can be easily removed during postprocessing. However, these corruptions are more difficult and computationally more intensive to remove from directly measured images. In addition, once wavefronts are collected, far-field effects can be computed for different apertures and a wide range of wavelengths, including the infrared range, where direct far-field studies require specialized optics and cameras. Thus, in the authors' opinion, the presented work provides a new opportunity to study and ultimately to compensate for aero-optical image distortion effects in airborne imaging and directed energy system applications.

Acknowledgments

This manuscript was a significantly modified and extended version of a SPIE conference paper by M. Kalensky, J. Wells, E. J. Jumper, and S. Gordeyev titled, "Image degradation due to various aero-optical environments," *SPIE Proceedings*, Vol. 11102, *Applied Optical Metrology III*; 111020F, 2019, <https://doi.org/10.1117/12.2528509>. The authors would like to thank Professor Eric J. Jumper for his useful comments about the manuscript. In addition, the authors would like

to thank Aaron Archibald from AFIT for his help in developing the tracker systems and for actively participating in imaging flight tests. This work was supported by the Joint Technology Office, Grant No. FA9550-13-1-0001 and Office of Naval Research, Grant No. N00014-18-1-2112. The U.S. Government was authorized to reproduce and distribute reprints for governmental purposes notwithstanding any copyright notation thereon.

References

1. E. J. Jumper and S. Gordeyev, "Physics and measurement of aero-optical effects: past and present," *Annu. Rev. Fluid Mech.* **49**, 419–441 (2017).
2. M. Wang, A. Mani, and S. Gordeyev, "Physics and computation of aero-optics," *Annu. Rev. Fluid Mech.* **44**, 299–321 (2012).
3. V. I. Tatarski, *Wave Propagation in a Turbulent Medium*, McGraw-Hill Book Company, New York (1961).
4. E. J. Jumper et al., "Airborne aero-optics laboratory," *Opt. Eng.* **52**(7), 071408 (2013).
5. E. J. Jumper et al., "Airborne aero-optics laboratory—transonic (AAOL-T)," AIAA Paper 2015-0675 (2015).
6. M. Kalensky, S. Gordeyev, and E. J. Jumper, "In-flight studies of aero-optical distortions around AAOL-BC," AIAA Paper 2019-3253 (2019).
7. M. R. Whiteley and D. J. Goorskey, "Imaging performance with turret aero-optical wave-front disturbances," *Opt. Eng.* **52**(7), 071410 (2013).
8. S. Gordeyev et al., "Image blurring due to turbulent wakes for airborne systems: flight tests," *Proc. SPIE* **10408**, 104080M (2017).
9. Y. Diskin et al., "Image blurring due to turbulent wakes for airborne systems: simulation and modeling," *Proc. SPIE* **10408**, 104080N (2017).
10. S. Gordeyev et al., "Aero-optical mitigation of shocks around turrets at transonic speeds using passive flow control," AIAA Paper 2013-0717 (2013).
11. E. J. Fitzgerald and E. J. Jumper, "The optical distortion mechanism in a nearly incompressible free shear layer," *J. Fluid Mech.* **512**, 153–189 (2004).
12. M. C. Roggemann and B. M. Welsh, *Imaging Through Turbulence*, CRC Press, New York (1996).
13. S. Gordeyev, J. Cress, and E. Jumper, "Far-field laser intensity drop-outs caused by turbulent boundary layers," *J. Dir. Energy* **5**(1), 58–75 (2013).
14. M. Kemnetz, "Analysis of the aero-optical component of jitter using the stitching method," PhD Dissertation, University of Notre Dame (2019).
15. C. Porter, S. Gordeyev, and E. Jumper, "Large-aperture approximation for not-so-large apertures," *Opt. Eng.* **52**(7), 071417 (2013).
16. S. Gordeyev et al., "Experimental studies of aero-optical properties of subsonic turbulent boundary layers," *J. Fluid Mech.* **740**, 214–253 (2014).
17. J. P. Siegenthaler, "Guidelines for adaptive optic correction based on aperture filtration," PhD Dissertation, University of Notre Dame (2009).
18. J. Siegenthaler, S. Gordeyev, and E. Jumper, "Shear layers and aperture effects for aero-optics," AIAA Paper 2005-4772 (2005).
19. M. R. Kemnetz and S. Gordeyev, "Optical investigation of large-scale boundary-layer structures," AIAA Paper 2016-1460 (2016).
20. K. Wang and M. Wang, "Aero-optics of subsonic turbulent boundary layers," *J. Fluid Mech.* **696**, 122–151 (2012).

Matthew Kalensky is a graduate researcher in the Department of Aerospace and Mechanical Engineering at the University of Notre Dame. He is a member of the Aero-Optics Group, where he is heavily involved in the group's airborne research platform, AAOL-BC. His research interests include but are not limited to aero effects, atmospheric propagation, beam control, and hypersonic propulsion.

Jonathan Wells is a graduate researcher in the Department of Aerospace and Mechanical Engineering, University of Notre Dame. He is a member of the Aero-Optics Group, where

he is involved in the group's airborne research platform, AAOL-BC. His research interests include thermodynamics, CFD, beam control, and atmospheric studies.

Stanislav Gordeyev is an associate professor at Department of Aerospace and Mechanical Engineering, University of Notre Dame, and a codirector of the Aero-Optics Group. His research interests include experimental investigation of optical distortions caused by compressible turbulent flow, both canonical and around complex geometries, like side-mounted turrets. He is also actively involved in aero-optical and reduced-order modeling, imaging at hypersonic speeds and flow control.